The effect of sample edge recombination on the averaged injection-dependent carrier lifetime in silicon

Michael Kessler, Tobias Ohrdes, Pietro P. Altermatt, and Rolf Brendel

The effect of sample edge recombination on the averaged injection-dependent carrier lifetime in silicon

Michael Kessler,[1,a)] Tobias Ohrdes,[1] Pietro P. Altermatt,[2] and Rolf Brendel[1,2]

[1]*Institute for Solar Energy Research Hamelin (ISFH), Am Ohrberg 1, Emmerthal 31860, Germany*
[2]*Department of Solar Energy, Institute of Solid-State Physics, Leibniz University of Hannover, Appelstr. 2, Hannover 30167, Germany*

In semiconductors, the effective excess carrier lifetime, τ_{eff}, measured in dependence on the injection density, Δn, is an important parameter. It is frequently observed that τ_{eff} decreases with decreasing Δn at low-level injection conditions (where Δn is smaller than the dopant density N_{dop}), which has been difficult to explain. We compare measurements with numerical device simulations to demonstrate that this observed reduction of τ_{eff} is caused by a combination of (i) Shockley-Read-Hall (SRH) recombination at the edges of the sample and (ii) transport effects of the carriers toward the edges. We measure $\tau_{\text{eff}}(\Delta n)$ of boron-diffused and surface-passivated p^+np^+ and p^+pp^+ silicon wafers with the commonly applied photo-conductance decay technique, and we vary the sample size. The photo-conductance is probed by inductive coupling within a sample region of about 3×3 cm^2; hence, the measurements yield an average value of both $\tau_{\text{eff,av}}$ and Δn_{av} within that region. For a detailed analysis, we determine τ_{eff} with a high spatial resolution using the dynamic infrared lifetime mapping technique, which shows a strong decrease of τ_{eff} toward the edges of the p^+np^+ samples at low-level injection. We analyze the measurements by numerical device modeling and circuit simulation. We conclude that the sample size should be at least 6×6 cm^2 for reliable $\tau_{\text{eff}}(\Delta n)$ measurements at low injection conditions. However, at high-injection conditions, the recombination usually dominates at the dopant-diffused surfaces. Therefore, the saturation current-density, J_0, can be extracted from the $\tau_{\text{eff}}(\Delta n)$ measurements in samples as small as 3×3 cm^2, with a measurement error due to edge recombination below 10%. © *2012 American Institute of Physics*. [http://dx.doi.org/10.1063/1.3691230]

I. INTRODUCTION

A reduction of the effective excess carrier lifetime, τ_{eff}, at low injection levels (LLI) strongly affects the solar cell performance at low illumination conditions.[1,2] The reduced τ_{eff} may result from enhanced recombination in the silicon bulk or at diffused or non-diffused surfaces in LLI. Often, τ_{eff} is measured to decide upon solar cell optimization strategies, and it is, therefore, important to exclude the possibility of any measurement artifacts, such as depletion region modulation (DRM)[3,4] or carrier trapping.[5] We show in this paper that, for certain sample structures, a minimum sample size is a crucial requirement for a correct injection-dependent τ_{eff} determination, especially when the measurement method does not yield local lifetime values, but averages over a certain area.

The overall recombination rate, R_{total} (Δn) (in units cm^{-3}s^{-1}), of any square sample is the sum of the recombination rate within the silicon bulk, $R_{bulk}(\Delta n)$, at the front and rear surfaces $R_{front}(\Delta n)/W + R_{rear}(\Delta n)/W$ and the surfaces at the edges of the sample $R_{edge}(\Delta n) \times W/l^2$,

$$R_{total}(\Delta n) = R_{bulk}(\Delta n) + \frac{R_{front}(\Delta n) + R_{rear}(\Delta n)}{W}$$
$$+ \frac{WR_{edges}(\Delta n)}{l^2}. \quad (1)$$

W is the thickness and l the edge length of a square sample (with $l \gg W$). R_{front}, R_{rear}, and R_{edge} are surface recombination rates in units cm^{-2}s^{-1} that correspond to the parallel surfaces of the sample and to the 4 edge surfaces of the sample, respectively. For large samples and/or for a low R_{edge}, the recombination at the edges of the sample can be neglected when measuring τ_{eff}. In fact, for many published lifetime data, R_{edge} has been neglected, as it was assumed that the overall recombination is dominated by the recombination at the front and rear surfaces and/or the recombination within the silicon bulk. However, for samples with high bulk lifetime and well-passivated front and rear surfaces, the recombination at the edge contributes significantly to the total recombination.

Reduced τ_{eff} in LLI are found in the literature for various silicon sample configurations: For example, Kerr and Cuevas[6] used *p*- and *n*-type samples in a wide range of base resistivities passivated with SiN_x and SiO_2.[7] Only for the *p*-type samples, they measured a reduced τ_{eff} in LLI for both passivation schemes. Steingrube *et al.*[8] explain these experimental results with a damaged region near the surface resulting from the SiN_X deposition or the pre-treatment of the wafer. Cousins and Cotter[9] measure reduced τ_{eff} in LLI for boron-diffused p^+pp^+ and phosphorus-diffused n^+pn^+ samples. They explain the reduced τ_{eff} in LLI with asymmetric capture cross-sections of SRH recombination within the bulk region resulting from the heavy boron and phosphorus diffusion process. Further injection-dependent lifetime data can be found in Refs. 10 and 11, and 12. Most of these samples have either a dopant-diffused or a charge-induced pn-junction. The sample size and possible resulting 2D effects due to possible enhanced recombination at the edges have not

a)Electronic mail: kessler@isfh.de.

been addressed, because these effects were assumed to be negligible.

It is well known that edge recombination not only affects τ_{eff} measurements for certain sample structures, but, for certain designs, also solar cell performance. The influence of edge recombination on solar cell performance was investigated by various authors: Hermle et al.,[1] Catchpole et al.,[2] Kühn et al.,[13] König and Ebest,[14] and McIntosh and Honsberg[15] investigated the effect of edge recombination by comparison of experimental and simulated solar cell parameters; for insufficiently passivated surfaces, all authors found a loss in V_{OC} as well as in fill factor (FF), and Hermle et al. as well as Catchpole et al. showed that the losses increase toward low illumination intensities (which corresponds to low injection levels).[1,2] Suggestions to reduce the effect of edge recombination are presented by König and Ebest[14] by introducing a novel grid concept and by Glunz et al.,[16] who suggested careful design optimization at the sample edge to ensure high efficiencies at low illumination intensities. Abbott et al.[17] investigated the effect of edge recombination via photoluminescence images and showed injection-dependent τ_{eff} for silicon samples with damaged pn-junction, but did not show a detailed analysis of the reason for the injection dependency. Chen and Cotter[18] showed decreased quasi-steady-state photoconductance (QSSPC) and quasi-steady-state photoluminescence (QSSPL)-measured $\tau_{eff,av}$ values in LLI for a p^+nn^+ sample structure, where they intentionally damaged the pn-junction with a laser groove in the center of their sample. They reproduced their measured $\tau_{eff,av}(\Delta n_{av})$ data with circuit simulation using a "resistively limited enhanced recombination" model from Ref. 19 and adding an additional recombination path (J_{02}).

In this paper, we concentrate on the influence of edge recombination on τ_{eff} measurements and demonstrate that the recombination at the edges during experimental τ_{eff} determination is not negligible for certain sample structures. In Sec. II, we measure $\tau_{eff}(\Delta n)$ of p^+np^+ samples with a pn-junction and p^+pp^+ samples with high-low junction and we vary the size of the sample. We determine τ_{eff} in LLI as well as in high-level injection (HLI), and we also extract the saturation current densities J_0 of the diffused regions. The local τ_{eff} for different injection levels is measured using the WCT-120 lifetime tester from Sinton instruments[20] as well as a camera-based dynamic infrared lifetime mapping (dynILM) measurement setup.[21] In Secs. III and IVs, we reproduce our measured values with numerical device simulations in two dimensions and with circuit simulation.

II. LIFETIME MEASUREMENTS

A. Sample preparation

Our silicon wafers were Cz-grown n-type (1.5 Ωcm) and FZ p-type (1.4 Ωcm) with a thickness of 300 $\pm$ 10 μm and a diameter of 6 in.es. These wafers were cut to a 125 $\times$ 125 mm^2 pseudo-square by a laser with 1030 nm wavelength and a pulse duration of 10^{-6} s. The samples were then cleaned with the standard RCA procedure[22] and rinsed in de-ionized water. After drying in N$_2$, we performed an open-tube liquid-source BBr$_3$ boron diffusion. The drive-in sequence at 1000 $°$C for 85 min included a 60 min in situ oxidation

sequence to avoid the formation of an undesirable boron-rich layer during the process.[23] The resulting sheet resistance, measured on reference wafers, was 60 $\pm$ 5 $\Omega/\square$. The boron silicate glass (BSG) was subsequently removed in hydrofluoric acid. After an additional RCA cleaning step, we then passivated the boron-diffused surfaces with a 10-nm-thin Al$_2$O$_3$ layer in a plasma atomic-layer-deposition (plasma-ALD) reactor from Oxford. The samples were annealed at 425 $°$C in an N$_2$ atmosphere for 15 min to activate the passivation action. A 100-nm-thick SiN$_X$ layer with a refractive index of 2.05 was deposited onto the Al$_2$O$_3$ as a capping layer by plasma-enhanced chemical vapor deposition (PECVD) at a temperature T = 400 $°$C. We measured the τ_{eff} of the samples using the WCT-120 photo conductance lifetime tester. The 125 $\times$ 125 mm^2-sized samples were then cut to square samples with an edge length of 2.5, 4, or 6 cm by a disk laser with 1030 nm wavelength and a pulse duration of 10^{-6} s. Figure 1(a) shows a schematic cross-section of our samples, while Fig. 1(b) shows the boron profile measured with the electrochemical capacitance voltage method (ECV).[24]

B. Local lifetime mapping with dynILM

1. Infrared lifetime mapping (ILM)

In this paper, we use the camera-based infrared lifetime mapping (ILM) for local Δn mappings, from which we derive the local τ_{eff}.[21] A CCD camera detects photons with a wavelength of 4–5 μm that are emitted from a silicon sample after a modulated excitation. For excitation of the carriers,
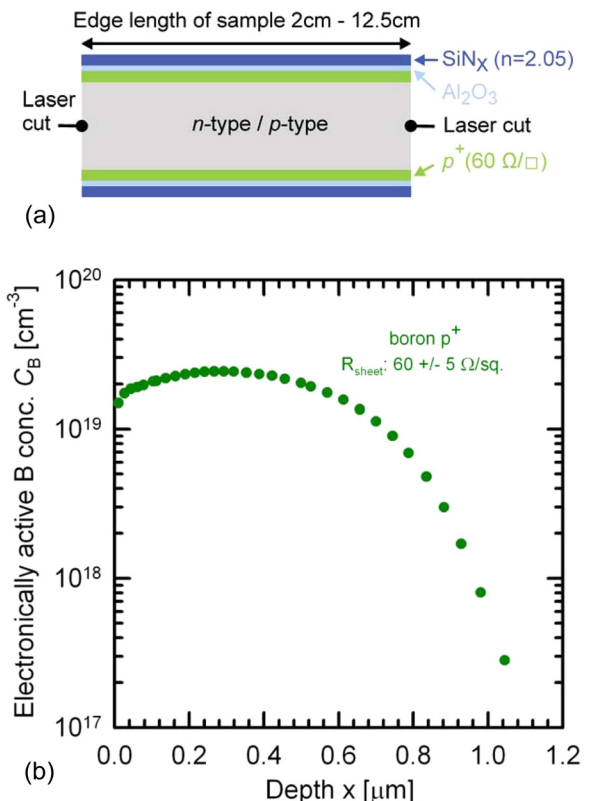

FIG. 1. (Color online) Schematic cross-section of the samples for lifetime measurements (a) and the boron profile (b) measured with the electrochemical capacitance voltage method (ECV) (Ref. 24).
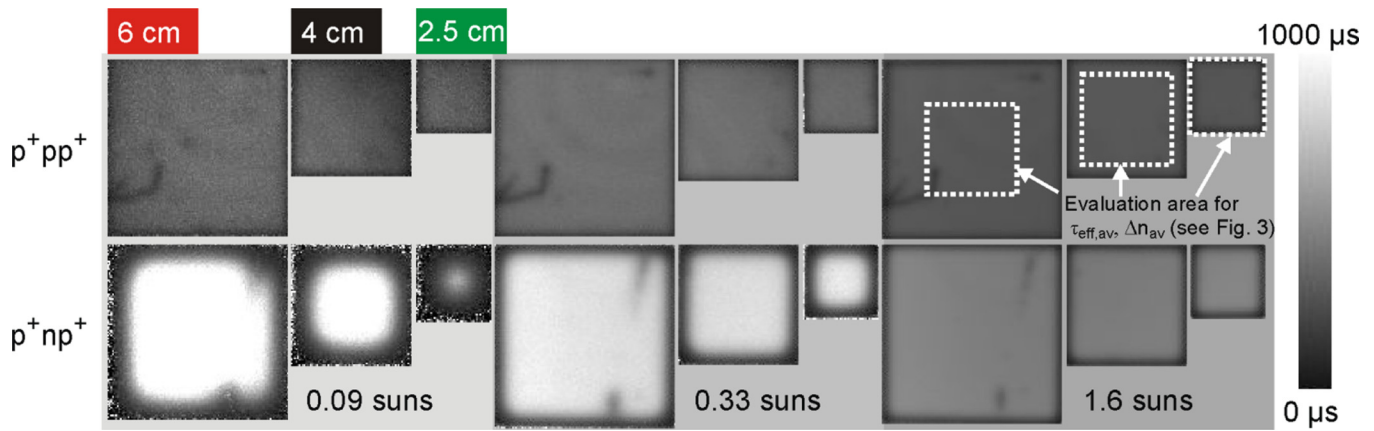
FIG. 2. (Color online) Effective carrier lifetime τ_{eff} of the p^+pp^+ and p^+np^+ samples with a side length of 6, 4, and 2.5 cm obtained by dynamic infrared lifetime mapping (dynIML) (Ref. 21) under an illumination intensity of 0.09, 0.33, and 1.6 suns, respectively. The indicated area of 3×3 cm^2 is used for the arithmetically averaged $\tau_{eff,av}$ shown as open symbols in Fig. 3.

we use a light-emitting diode (LED) array with a wavelength of 950 nm. The temperature of the sample during measurement is 70 °C in order to generate the free carrier emission signal. The camera signal is linked to the excess carrier concentration Δn via

$$\Delta n = \frac{S}{c}, \qquad (2)$$

where S is the camera signal and c is the calibration coefficient of the calibration curve, which is a constant for planar wafers. From the camera signal, S, one can derive the *local* Δn and, hence, the *local* τ_{eff} values with either the dynamic ILM (dynILM) or static ILM (sILM) approach. The dynILM method allows the calibration-free spatially resolved τ_{eff} determination.[21] The dynILM method uses a lock-in approach and *first* calculates the τ_{eff} using the integrated transient camera signal and the integration time: $\tau_{eff} = f(S_{tr}, t_{int})$. The corresponding local injection level Δn is then calculated by

$$\Delta n = \tau_{eff}G = \frac{\tau_{eff} \times \Phi_{suns}}{W}, \qquad (3)$$

where Φ_{suns} is the photon flux of 2.78×10^{17} photons per cm^2 at 1 sun intensity. The sILM approach firstly determines Δn by the relation from Eq. (2) and therefore requires a calibration relation. Based on Eq. (3), the τ_{eff} is then calculated by $\tau_{eff} = \Delta n/G$. For determination of the generation rate G, the short-circuit current J_{sc} of a calibrated reference solar cell is measured and a reasonable assumption on the front side reflectivity of the sample under test is made.[21]

One important issue for either ILM evaluation approach is the error in the local τ_{eff} and Δn values due to internal blurring for samples with regions of different local τ_{eff} and Δn; emitted photons propagate within the sample in the lateral direction due to internal reflection. Thus, they are emitted at a remote position of the sample in respect to the place where they are emitted. Therefore, the local τ_{eff} and Δn values are inaccurate; the error in the case of internal blurring for samples with adjacent regions of high and low lifetime was found to be significant within low lifetime regions for the dynamic ILM approach.[21] The error due to internal blurring is less pronounced for the sILM approach. We therefore use the sILM evaluation method for comparison of

circuit simulation with ILM-measured local τ_{eff} (Δn)-values, as the local τ_{eff} values at the sample edge is a crucial input parameter for our simulations. We use the dynILM method to compare ILM-measured τ_{eff} (Δn) values to the injection-dependent photoconductance decay (PCD)-measured $\tau_{eff,av}$ (Δn_{av}) values, as the dynILM is a fast and calibration-free approach.

For details of the ILM measurements apparatus and further details on the measurement principle, as well as the error due to internal blurring, see Refs. 21 and 25.

2. ILM measurements results

Figure 2 shows the locally resolved τ_{eff} of the p^+np^+ and p^+pp^+ samples with a side length of 6, 4, and 2.5 cm measured with the dynILM. Note that, in the p^+np^+ samples, τ_{eff} decreases strongly toward the edges at low carrier generation (0.09 and 0.33 suns), in contrast to the p^+pp^+ samples. Note also that, under 1.6 suns, the τ_{eff} of the p^+np^+ sample shows a less pronounced decrease toward the wafer edges for all sample sizes. Due to internal blurring, the τ_{eff} at the sample edge is *overestimated*. From comparison of dynILM and sILM data, we estimate that the local τ_{eff} is overestimated by a factor between 6 and 20 in a region of 2–5 mm close to the sample edge (see Sec. IV for sILM measurement results).

The area of 3×3 cm^2, indicated in Fig. 2 by dashed lines, is used for calculating the arithmetically averaged $\tau_{eff,av}$ for comparison with PCD measurements (see Sec. II C1). These $\tau_{eff,av}$ values are shown as open symbols in Fig. 3 at various Δn_{av} levels and will be compared to PCD further below. We do not have an exact knowledge about the local sensitivity of the silicon sample in respect to the PCD detection coil. However, averaging τ_{eff} over an area larger than the 3×3 cm^2 area indicated in Fig. 2 does not affect the qualitative behavior and would merely lead to a more pronounced decrease of $\tau_{eff,av}$ in low-level injection.

C. PCD lifetime measurements

1. Inductive coupling

Commonly, τ_{eff} is determined by inductively coupling a RF oscillating circuit to a silicon sample[26] for the detection
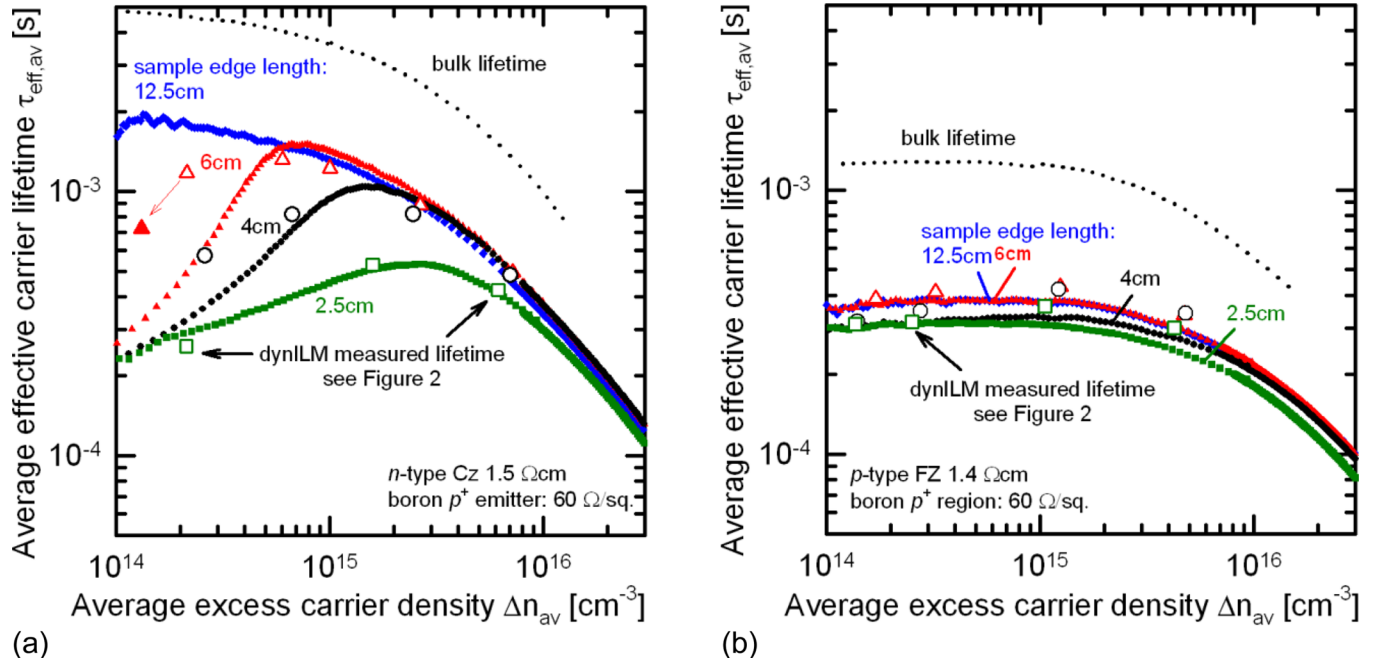
FIG. 3. (Color online) The effective average excess carrier lifetime, $\tau_{eff,av}$, of p^+np^+ (a) and p^+pp^+ (b) samples with varying sample size measured with the contactless photoconductance decay method (filled symbols) as well as with the dynamic infrared lifetime mapping (open symbols) averaged over the area indicated in Fig. 2. The lower limit of the bulk carrier lifetime, obtained from SiN_X-passivated reference samples, is indicated as dotted line.

of the photoconductance σ_{ph} (PC). For specific sample structures, it is thus possible to obtain information about the silicon bulk quality, the silicon surface passivation quality, and the recombination behavior of diffused surfaces.[27] Therefore, this method has found wide application in photovoltaics research and development as well as during in-line fabrication control.

The determination of σ_{ph} is done by inductively coupling a silicon sample to a radio frequency (RF) oscillating circuit. The oscillating magnetic field induces an eddy current within the silicon sample leading to Joule dissipation.[28] The absorbed power P_a depends on the local conductivity of the sample $\sigma(x, y, z)$, and is enhanced when any conductive material (e.g., a silicon sample) is placed close to the detection coil.[29] The absorbed power within the conductive material is

$$P_a = \int_V \sigma(x,y,z)\vec{E}(x,y,z)^2 dV, \qquad (4)$$

where $\vec{E}(x,y,z)$ is the local electrical field, which results from the time-dependent change in the magnetic flux density. The induced eddy current produces a magnetic field, which influences the RF circuit characteristics. This inductive coupling, which depends on the conductivity of the sample, can then be translated into an average time-dependent conductivity $\sigma(t) = \sigma_{ph}(t) + \sigma_0$ of the silicon sample via a calibration curve. Please note that the measured conductivity $\sigma(t)$ is averaged over a specific region near the coil, so that one always extracts the *averaged* values $\tau_{eff,av}$ and Δn_{av} with an inductive coupling apparatus. For details, see Ref. 28.

The $\tau_{eff,av}$ is given by $\tau_{eff,av} = \Delta n_{av}/G = \Delta n_{av}/R$ for the steady state condition or by $\tau_{eff,av} = -\Delta n_{av}/(d\Delta n_{av}/dt)$ in the transient case, where G and R are the generation or recombi-

nation rates, respectively. The average carrier concentration Δn_{av} within the silicon sample can be derived from

$$\Delta n_{av} = \frac{\sigma_{ph}}{qW(\mu_e + \mu_h)}, \qquad (5)$$

where σ_{ph} is the measured photogenerated excess conductivity, q is the elementary charge, while $\mu_e(\Delta n_{av})$ and $\mu_h(\Delta n_{av})$ are the electron and hole mobilities, respectively. A consistent solution for $\mu_e + \mu_h$ and Δn_{av} can be found iteratively for a chosen mobility model (frequently used models are Refs. 30–33).

2. Results

Figure 3 shows the $\tau_{eff,av}$ values obtained with the WCT-120 photo conductance lifetime tester. After calibration of the setup with the standard calibration procedure, we measure $\tau_{eff,av}$ using two white diffusers and the IR pass filter, as recommended by Sinton.[34] The results from both transient and quasi-steady-state (QSS) methods agree over the entire measurement range, as was also observed by Kerr.[7] Note that the QSSPC data require a scaling factor for the exact determination of the generated carriers within the sample, because there is $\tau_{eff,av} = \Delta n_{av}/G$ in steady state. We adjusted the QSS measured $\tau_{eff,av}$ values to the transient measured data by adjustment of the generation rate G as suggested by Sinton.[34]

At high injection levels ($\Delta n \geq 10^{16}$ cm^{-3}), we observe that τ_{eff} stays within 20% of the values initially measured at the uncut 125×125 mm^2 samples, as indicated in Fig. 3. This is observed for both samples types (with a pn-junction or a high-low junction). At these injection levels, the saturation current-density, J_0, of the dopant diffusions is extracted with the commonly used procedure of Kane and Swanson.[27] Table I lists these J_0 values obtained between $\Delta n = 1.4$

TABLE I. The saturation current density, J_0, of the dopant diffusion extracted from the measurements shown in Fig. 3 using the procedure of Kane and Swanson (Ref. 27). The given error accounts for **2%** uncertainty in the generation rate and for a **2%** uncertainty in the wafer thickness and does not include a possible systematic error, due to a varying Δn throughout the sample.

Sample size [cm]	p$^+$**n**p$^+$		p$^+$**p**p$^+$	
	1.5 Ωcm J_0 [fA/cm^2]	200 Ωcm J_0 [fA/cm^2]	1.4 Ωcm J_0 [fA/cm^2]	200 Ωcm J_0 [fA/cm^2]
12.5	55 ± 5	57 ± 5	56 ± 5	50 ± 5
6	53 ± 5	58 ± 5	55 ± 5	53 ± 5
4	55 ± 5	53 ± 5	53 ± 5	53 ± 5
3	56 ± 5	56 ± 5	56 ± 5	52 ± 5
2.5	55 ± 5	80 ± 8	61 ± 6	57 ± 5
2	112 ± 10	144 ± 15	118 ± 10	111 ± 10

$\times 10^{16}$ cm^{-3} and 2.6×10^{16} cm^{-3} and referred to an intrinsic carrier density n_i of 10^{10} cm^{-3}. Note that the J_0 values increase only for samples with an edge length below 3 cm. Reference samples with a base resistance of 200 Ωcm show consistent results. This implies that J_0 can be measured with a relative error below 10% if the sample size is larger than 3 cm, independently of the base resistance and sample structure (p$^+$pp$^+$ or p$^+$np$^+$).

Going from HLI ($\Delta n > 1 \times 10^{16}$ cm^{-3}) toward lower injection levels, $\tau_{\text{eff,av}}$ increases for both sample types and all sample sizes, due to a reduction in recombination rate at the boron-diffused, passivated surfaces[35] as well as reduced bulk Auger recombination losses.[36] Note that, toward low injection conditions, $\tau_{\text{eff,av}}$ reduces with smaller sample size, especially strongly in the samples with a pn-junction. The PCD- and dynILM-measured lifetimes are consistent apart

from the measured lifetime in LLI of the 4 and 6 cm^2 samples with a pn-junction. A possible explanation for this discrepancy is that the evaluation area for dynILM measurements of 3×3 cm^2 is not exactly identical to the sensitivity area of the detection coil used for PCD measurements. To demonstrate the influence of a change in evaluation area, we added one data point $\tau_{\text{eff,av}}$ (Δn_{av}) that we calculated from an area of 5×5 cm^2 (red filled triangle) in Fig. 3. We thus show that the assumed evaluation area is a crucial parameter for interpretation of the dynILM-measured τ_{eff} (Δn) and that an increase in evaluation area results in an decrease of $\tau_{\text{eff,av}}$ as well as Δn_{av}.

III. SIMULATION

We simulate the injection-dependent $\tau_{\text{eff,av}}$ with the numerical device simulator Sentaurus,[37] which solves the semiconductor differential equations self-consistently. Figure 4(a) shows our simulation domain, and the specific device parameters are listed in Table II. For symmetry reasons, a two-dimensional domain approximates the real situation sufficiently well. The domain spans half the sample width l from the symmetry point to the edge. The width of the domain relevant to the induction measurement via the indicated coil is indicated with x^* and is taken as 1.5 cm for all sample sizes. For samples with a sample size smaller than 3 cm, x^* is taken as $l/2$ The boron dopant profile from Fig. 1 is used at the front and rear surfaces, together with the surface recombination velocity parameter S_{surf} from Ref. 38. The S value at the sample edge, S_{edge}, may depend on the cleaving technique, such as laser cutting, sawing, etc., as well as on the applied etching procedures. We choose the thermal velocity (10^7 cm/s) as the
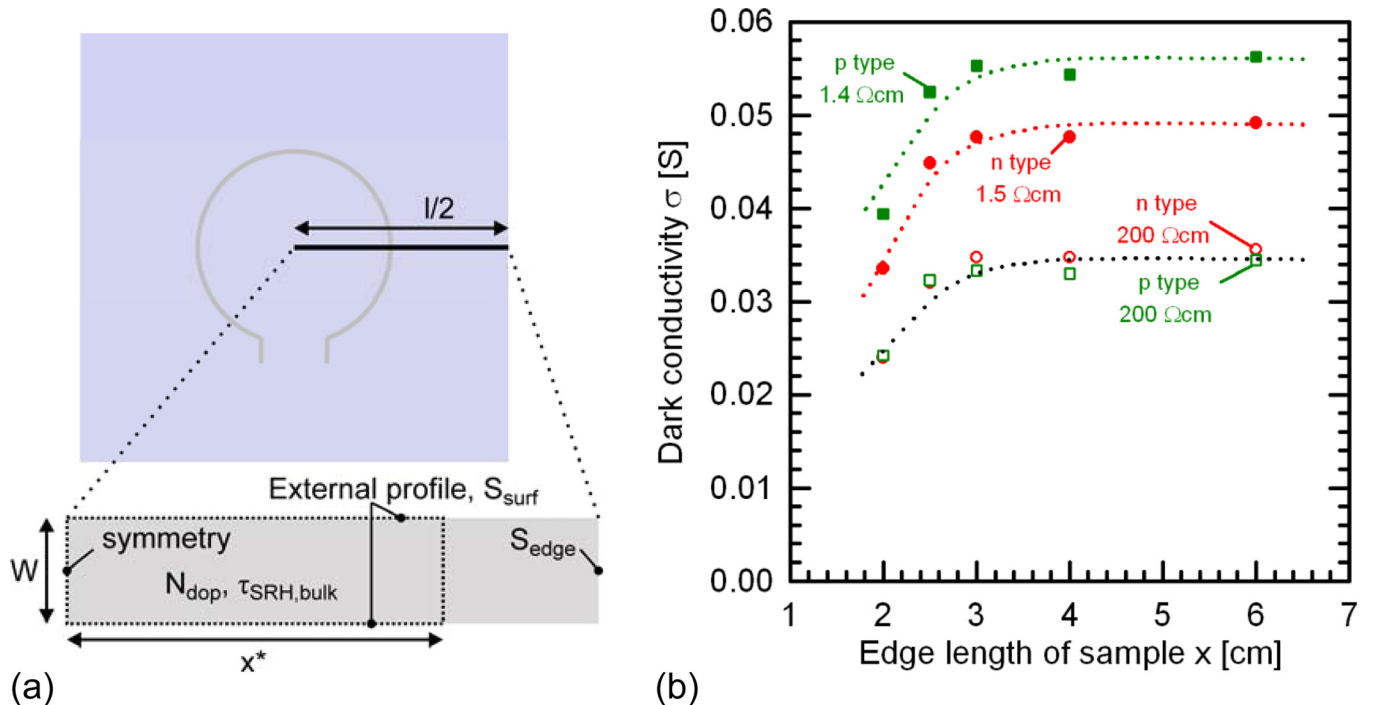

FIG. 4. (Color online) Simulation model for τ_{eff} calculation (a) and measured dark-conductivity of differently doped p$^+$pp$^+$ and p$^+$np$^+$ samples for the determination of the integration region in the simulations (b). The dotted lines are guides to the eyes only.

TABLE II. Input parameters for the numerical device simulation of the injection-dependent $\tau_{\text{eff,av}}$. All symbols are defined in Fig. 4(a).

Parameter	Unit	Sample structure	
		p^+np^+	p^+pp^+
$\tau_{\text{SRH,bulk}}$	μs	10 000[a]	1000[a]
S_{edge}	cms^{-1}	10^7	10^7
S_n	cms^{-1}	22	22
S_p	cms^{-1}	220	220
W	μm	300	300
l	cm	2–12.5	2–12.5
x^*	cm	1.5 if $l \geq 3$ cm	1.5 if $l \geq 3$ cm
		$l/2$ if $l < 3$ cm	$l/2$ if $l < 3$ cm
N_{dop}	cm^{-3}	Phos. 3×10^{15}	Boron 1×10^{16}

[a]Derived from bulk lifetime measurement shown in Fig. 3.

TABLE III. Input parameters for the numerical simulations shown in Fig. 6.

Parameter	Unit	Sample structure	
		p^+np^+	p^+pp^+
$\tau_{\text{SRH,bulk}}$	ms	10	10
S_{edge}	cms^{-1}	10^7	10^7
S_n	cms^{-1}	22	22
S_p	cms^{-1}	220	220
W	μm	300	300
l	cm	2.5	2.5
x^*	cm	1.25	1.25
N_{dop}	cm^{-3}	Phos. 5×10^{15}	Boron 5×10^{15}

upper limit. The remaining model parameters, such as the intrinsic density, etc., are given in Table III of Ref. 39.

Figure 4(b) shows the dark conductivity for various edge lengths measured with the WCT-120 photo conductance lifetime tester.

The measured conductivity increases with increasing sample size and reaches a saturation value for an edge length $l \geq 3$ cm. This is so because the sensitivity of the detection coil is limited to a certain area, as indicated in Sec. II (Eq. (4)). We therefore chose this edge length and the resulting area as the integration area for our simulated Δn_{av} and $\tau_{\text{eff,av}}$ values. In order to vary Δn_{av}, we vary the locally homogenous generation rate, which corresponds to a carrier excitation by long wavelength photons. We choose a homogenous local generation, as both dynILM and QSSPC measurements are performed with long wavelength photons. However, our test simulations show that we achieve identical simulation results (in terms of carrier lifetimes) using an

am1.5 g spectrum.[40] We then extract the average injection level $\Delta n_{\text{av}} = \int_A (n - n_0) \cdot dA$ and the average generation rate from each steady state solution to compute the average effective excess carrier lifetime,

$$\tau_{\text{eff,av}} = \frac{\int_A (n - n_0) \cdot dA}{\int_A G \cdot dA}, \tag{6}$$

where $A = W \times x^*$ is the cross section area of the sample.

The lines in Fig. 5 show the simulated $\tau_{\text{eff,av}} (\Delta n_{\text{av}})$ for both the p^+np^+ and the p^+pp^+ samples with various sample sizes. The corresponding experimental $\tau_{\text{eff, av}}$ for the samples with 2.5, 4, 6, and 12.5 cm edge length, respectively, are included from Fig. 3 for comparison.

The simulated $\tau_{\text{eff,av}}$ fits the experimental data well, except that the simulated $\tau_{\text{eff,av}}$ in LLI is consistently higher than the measured lifetime for the p^+np^+ sample with an edge length of 6, 4, and 2.5 cm. This is probably caused by the following two approximations in our simulation model: (i) in our two-dimensional approximation, we model only a slab with one edge, while in the three-dimensional experiment, the recombination occurs at the entire surrounding of the sample.
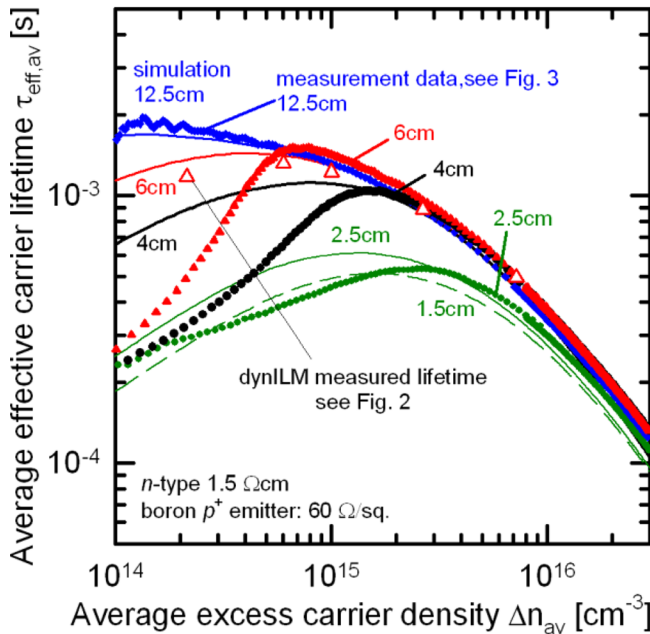
(a)
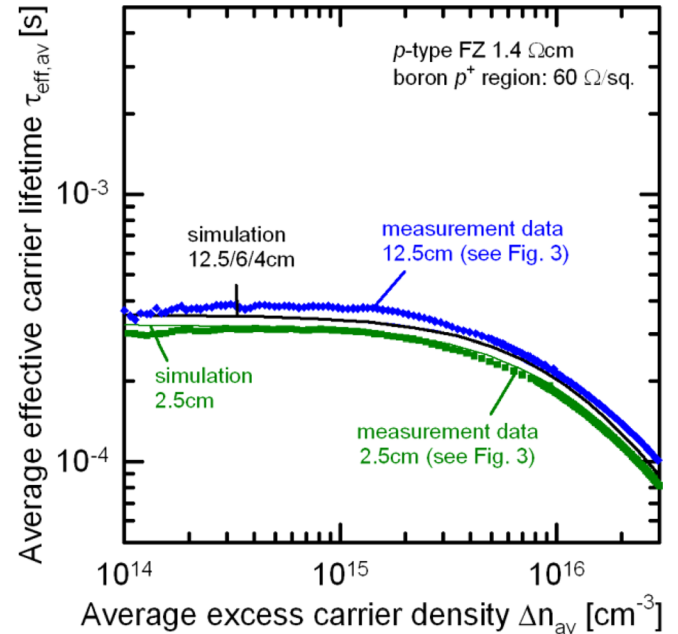
(b)

FIG. 5. (Color online) Simulated effective average excess carrier lifetime, $\tau_{\text{eff,av}}$, of p^+np^+ (a) and p^+pp^+ (b) samples (lines). Measurement data from the samples with 2.5, 4, 6, and 12.5 cm edge length, respectively, are included for comparison (symbols).
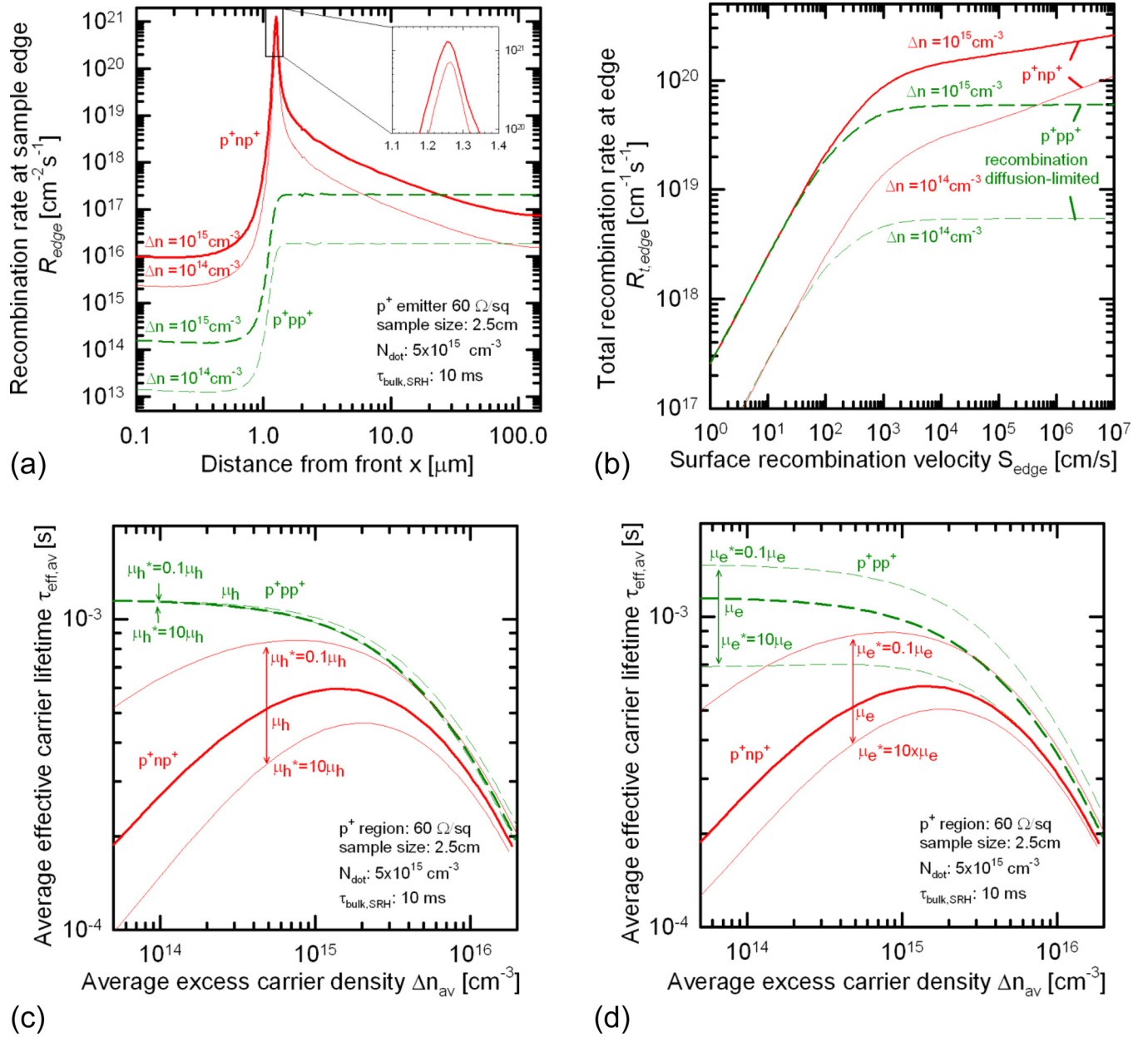
FIG. 6. (Color online) Upper figures: simulated local recombination rate, R_{edge}, at the sample edge as a function of position (a) and total recombination rate at the wafer edge in the p^+np^+ samples (red solid lines) and the p^+pp^+ samples (green dashed lines) as a function of the surface recombination velocity, S_{edge}, (b) at two different average injection levels. The lower figures show the corresponding $\tau_{eff,av}$ using a modified hole mobility (c) or electron mobility (d).

(ii) The integration region $W \times x^*$ for averaging $\tau_{eff,av}$ in our simulation might exceed the experimentally determined region of sensitivity for our PCD measurement setup of approximately 3×3 cm^2. Both effects lead to an underestimation of the recombination at the edges in our simulations.

IV. INTERPRETATION

Our experimental investigation and numerical simulation show that increased recombination at the sample edges lead to reduced $\tau_{eff,av}$ in LLI for p^+np^+ samples. For a more detailed analysis, we now present numerical simulations to elucidate which part of the edges contributes dominantly to the enhanced recombination and why this recombination is not as pronounced when going to high injection densities.

Additionally, we present circuit simulations to explain how carrier transport toward the edges influences the injection-dependent $\tau_{eff,av}$.

We use the model introduced in Sec. IV, but apply identical wafer-doping densities $N_{boron} = N_{phos} = 5 \times 10^{15}$ cm^{-3} as well as an identical bulk lifetime parameter $\tau_{SRH,bulk}$. The edge length l is 2.5 cm, and we choose the p^+ diffusion profile from Fig. 1. The parameters we used in these simulations are summarized in Table III.

A. Injection dependency

Figure 6(a) shows the simulated recombination rate, R_{edge}, at the sample edge in dependence of the distance from the silicon surface up to $W/2$ for two different average

injection levels Δn_{av}: 1×10^{14} cm^{-3} and 1×10^{15} cm^{-3}. Note that the recombination rate within the space charge region (SCR) is up to 5 orders of magnitude higher in the p-n junction of the p$^+$np$^+$ sample than in the high-low junction of the p$^+$pp$^+$ sample. This is so because, in SRH theory, the maximum recombination rate occurs at the position where[41]

$$nS_n = pS_p, \tag{7}$$

which means near the point where $n \approx p$. This condition exists in the pn-junction, but not in the high-low junction, and it is the main reason why samples with a pn-junction suffer from considerably more recombination losses at the edges than samples with a high-low junction. This peak in recombination becomes less pronounced toward HLI, because the carrier densities near the point where $n \approx p$ increase significantly slower than in the quasi-neutral region of the wafer.[41] Specifically, while going from the lower to the higher Δn_{av} in Fig. 6(a), there is a fourfold increase in the recombination rate in the quasi-neutral regions (at $x = 0.1$ μm and $x = 150$ μm), but there is only a 1.75-fold increase in recombination where $n \approx p$ within the space charge region (see inset in Fig. 6(a) at $x = 1.26$ μm). We cannot verify at this point if the described change in recombination for a change in injection level within the SCR is dominantly caused by transport effects or by recombination effects within the SCR.

Using numerical simulations, Hermle *et al.*[1] also showed that, when going from 1-sun illumination to low illumination intensities (1/100 suns), the recombination within the SCR decreases less strongly than the recombination within the quasi-neutral regions. Stellwag *et al.*[42] showed similar result for GaAs-based solar cells; the ratio of recombination within the SCR and recombination within the quasi-neutral regions is increasing for a decreasing bias voltage.

For a reduced Δn_{av} of 1×10^{14} cm^{-3}, the recombination within the diffused region ($x < 1$ μm) at the sample edge is reduced in both sample structures. The low recombination rate of the p$^+$np$^+$ sample (compared to the p$^+$pp$^+$ sample) at the sample edge for $x > 50$ μm can be explained by a non-uniform carrier distribution within the bulk of the n-type samples; the strongly enhanced recombination at the pn-junction leads to carrier gradients and a resulting non-uniform carrier distribution within the sample.

B. Carrier transport effects

The recombination at the edge depends not only on the recombination velocity, S_{edge}, but also on the supply of carriers. To distinguish between these two influences, we now vary S_{edge} in Fig. 6(b) at the two different average injection levels of Sec. IVA (1×10^{14} cm^{-3} and 1×10^{15} cm^{-3}) and plot the total recombination rate at the edge $R_{t,edge}$ (integrated over the edge length l). In the p$^+$pp$^+$ samples, the $R_{t,edge}$ saturates at $S_{edge} > 5000$ cm/s. This indicates that the recombination at the edge becomes limited by the transport of carriers toward the edges. Varying the hole or the electron mobility in Figs. 6(c) and 6(d), it becomes apparent that the limiting transport mechanism is diffusion of electrons in the quasi-neutral base region. As the electron diffusion length is (1.2 ± 0.1) mm, the recombination at the edge is negligible compared to the entire sample, which is consistent with our $\tau_{eff,av}$ measurements. In contrast, $R_{t,edge}$ keeps increasing at $S_{edge} > 5000$ cm/s in Fig. 6(a) in the case of the p$^+$np$^+$ samples, although the hole diffusion length within the n-type base is (3.8 ± 0.5) mm. Figures 6(c) and 6(d) show that $R_{t,edge}$ is sensitive to both electron and hole mobility, and Figs. 7(a) and 7(b) show that the holes are transported to the edge mainly as majority carriers via the p$^+$ region and the electrons mainly as majority carriers via the n-type base region. Hence, the carriers are transported to the edge via drift and there is no limitation by diffusion. This enables a very efficient carrier transport, making pn-junction devices even more prone to recombination at the edges than samples with a high-low junction. Note, in Figs. 7(a) and 7(b), that the carriers are injected across the junction very close to the edge, so both majority and minority carriers are supplied mainly by drift.
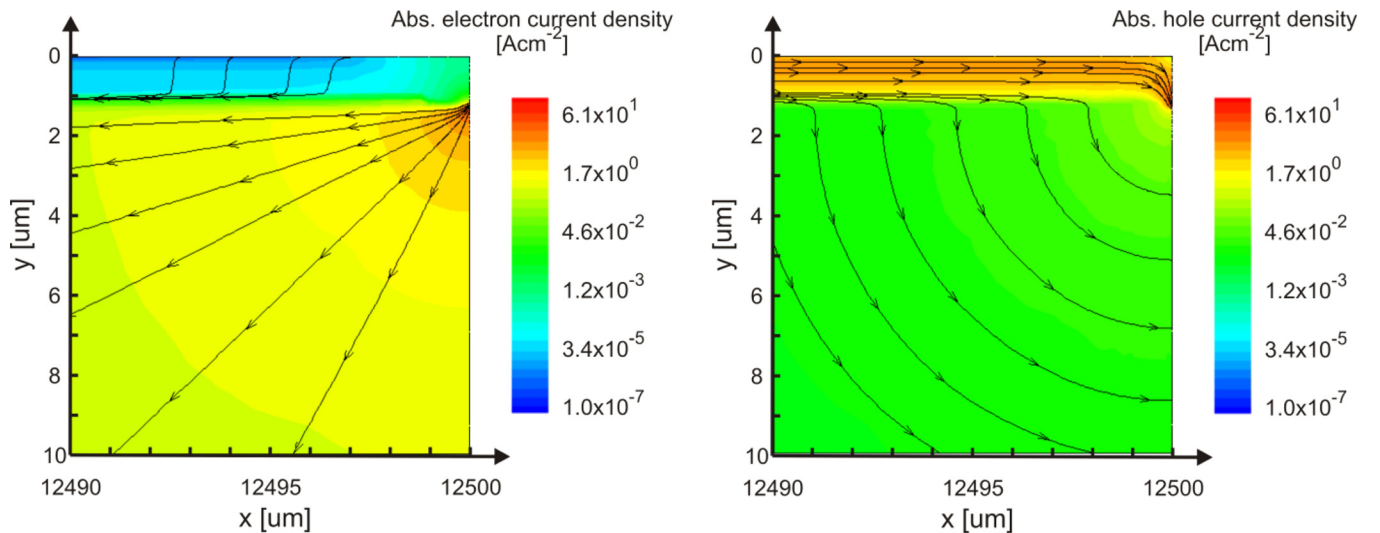

FIG. 7. (Color online) Simulated electron (a) and hole (b) current-densities within a 10×10 μm^2 region at the corner of the p$^+$np$^+$ sample. Note that the arrows of electron flow point in the reverse direction (because the charge is negative). The junction is about 1.3 μm below the top surface.

C. Circuit simulations

In the p^+np^+ sample, the carriers required for recombination at the edges are predominantly supplied as majority drift currents. With numerical device simulation, we are able to explain the recombination behavior of p^+np^+ and p^+pp^+ samples at different injection levels, but we cannot separate transport and recombination effects explicitly. To elucidate how recombination at the edge is influenced by the transport properties, we now perform circuit simulations. Figure 8 shows the schematic of our circuit. Our simulation domain describes the upper side of one half of the cross section of our 2.5×2.5 cm^2 sample. The circuit consists of 125 identical elements, each representing a 100×150 μm^2 cross section of the 1.25×0.015-cm-wide simulation domain. The diodes are represented by the Shockley diode equation: $J = J_0 (\exp(V/V_{th})-1) - J_{sc}$, where the thermal voltage $V_{th} = 25.69$ mV (at 25 °C).

$R_{base} = 2 \times \rho/W$ represents the n-type base resistance for electrons with $\rho = 1.5$ Ωcm ($N_{dop} = 3.23 \times 10^{15}$ cm^{-3}) and $W/2 = 0.015$ cm. R_{diff} is the resistance of holes within the diffused p^+ region below the Si surface and is given by the measured sheet resistance of 60 $\Omega/\square$ (see Sec. II). We like to compute V_{ab} across the pn-junction as a function of x (with the edge at $x = 0$) and to compare it with $\Delta n(x)$ measured by sILM. We therefore express $\Delta n(x)$ as local voltage, $V_{jctn}(x)$, across the pn-junction using

$$V_{jctn}(x) = V_{th} \cdot \ln\left(\frac{(\Delta n(x) + N_{dop}) \times \Delta n(x)}{n_i^2}\right). \quad (8)$$

According to the sILM-measured $\tau_{eff} = 16$ μs at the sample edge (for G = 0.18), the external voltage $V_{ab}(x = 0) = 528$ mV for G = 0.18. We intentionally assume the identical *constant* lifetime $\tau_{eff} = 16$ μs at the sample edge for G = 0.75 so that $V_{ab}(x = 0) = 566$ mV. The actual sILM-measured τ_{eff} at the sample edge for generation rate of G = 0.75 is (50 ± 10) μs, but we neglect this injection dependency of τ_{eff} at the sample edge, which results from the effect of a changing recombination situation within the SCR at the sample edge, as discussed in Sec. IV. It is not our intention to use a more sophisticated boundary condition at $x = 0$, like a combination of J_{01} and J_{02} diodes in our circuit simulation, like in Ref. 18. Thus, we exclusively concentrate on transport effects in our circuit simulations. All injection dependencies can therefore be assigned to be a result of carrier transport, due to the above-discussed assumption of a constant τ_{eff} at the sample edge. J_0 and J_{SC} are the diode saturation currents and the generated photo-currents within the sample. We use the measured J_0 values from Table I

(55 fA/cm^2) and consider a carrier generation rate we used in our ILM measurements of G = 0.18 and 0.75 suns, respectively, which correspond to a J_{sc} of 8.02 mA/cm^2 and 33.4 mA/cm^2, respectively.

We vary the injection level by varying J_{sc}, and we extract $V_{jctn}(x)$ as a function of the position x in our circuit. Figure 9(a) shows the simulated V_{jctn} obtained by using SpiceGUI[43] compared to $V_{jctn}(x)$ implied from our sILM measurements of $\Delta n(x)$ using Eq. (8). At the lower illumination level, both the simulated and the measured local voltages across the pn-junction decline at $x < 1$ cm, while for the higher level, they decline in a smaller region (at $x < 0.6$ cm). Our circuit simulations explain the measured injection dependencies of $\tau_{eff,av}$ qualitatively. We conclude that *majority* carrier transport toward the recombination active SCR at the sample edges is a crucial parameter for the measured and simulated injection dependencies. Note that our circuit simulations do not include any bulk recombination effects and that there is an inaccuracy when determining the voltage for $x = 0$ due to an inaccuracy in the ILM-measured lifetime. However, the tendency of an increasing influence of edge recombination toward lower injection levels can be described properly with our circuit simulations.

In further circuit simulations, we vary the bulk and emitter resistance to show the effect of a lightly doped base material and lightly doped emitters (such as charge-induced inversion emitters); the results are included in Fig. 9(a) and shown in Fig. 9(b). Both an increasing sheet and bulk resistance results in a steeper characteristic of V_{ab} (x). The region with constant voltage (which corresponds to a constant lifetime) is increasing for (i) an increasing generation rate, (ii) an increasing sheet resistance, and (iii) an increasing bulk resistance. This result given indicates that edge recombination effects explain injection dependencies of measured area averaged effective excess carrier lifetimes only for certain sample structures, sample size, and with a particular bulk and emitter resistance.

From our circuit simulation results, it is possible to calculate a corresponding $\tau_{eff,av}$ versus Δn_{av} plot. We calculate $\Delta n(x)$ from $V_{jctn}(x)$ by Eq. (8) and derive Δn_{av} by taking the arithmetic mean of the simulated $\Delta n(x)$ obtained at various illumination intensities. There is $\tau_{eff,av} = \Delta n_{av}/G$ with $G = J_{sc}/ (W \times q)$. The resulting injection-dependent $\tau_{eff,av}$ is shown in Fig. 10 for a variation of τ_{eff} at the sample edge (a) and for a variation in sample size (b). For the simulation of the sample without any edge recombination, we use $V_{ab}(x = 0) = V_{th} \times \ln (J_{sc} /J_0 + 1)$ as a boundary condition (dashed black line). Note that, for our simulation shown in Fig. 10(b), we average $\Delta n(x)$ over the entire sample size, which is not consistent to our numerical simulation, where we limited the section for evaluation to an area of 3×3 cm^2. Therefore, we underestimate the $\tau_{eff,av}$ values in LLI for the sample size 4, 6, and 12.5 cm in respect to our numerical simulations.

The injection-dependent τ_{eff} of the PCD as well as dynILM measured data (see Fig. 10(a)) is qualitatively consistent with the values from our circuit simulation. Nevertheless, experimental and simulated data do not fit quantitatively, due to a number of simplifications in our circuit model; we do
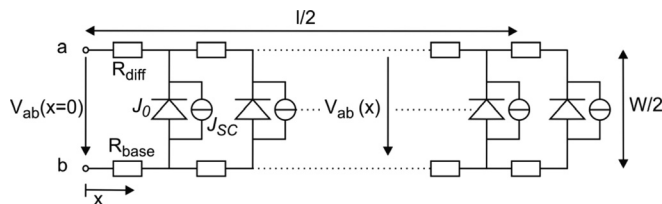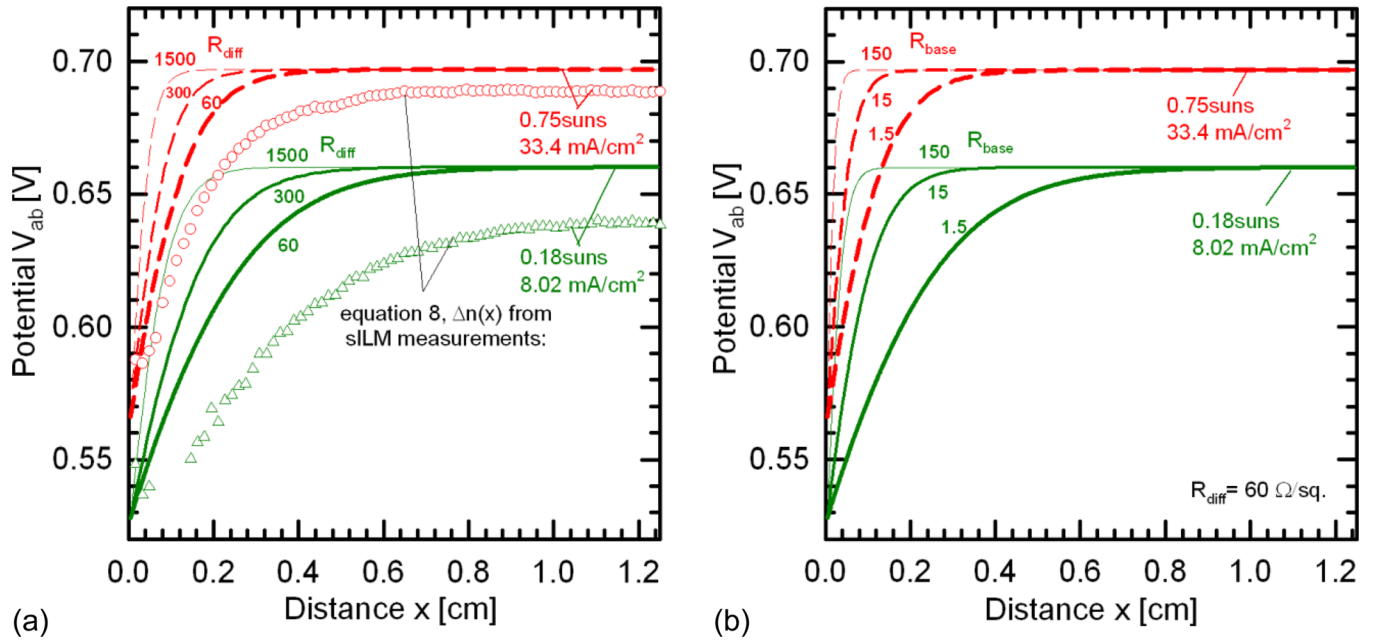

FIG. 8. Circuit model for investigating the majority carrier transport effects. $x = 0$ is the edge of the sample with thickness, W, R_{diff} the resistance in the boron-diffused region, R_{base} the resistance in the n-type base region.

FIG. 9. (Color online) The local voltage across the pn-junction in the 2.5×2.5 cm^2 p$^+$np$^+$ sample obtained by circuit simulations (lines) and implied via Eq. (8) from $\Delta n(x)$-measurements using sILM (symbols) at two different illumination levels (0.18 and 0.75 suns). Simulation results are shown for a variation of (a) the sheet resistance R$_{diff}$ of the boron-diffused region and (b) the bulk resistivity, R_{base}.

not consider (i) any bulk recombination effects, like Auger recombination, and (ii) any injection-dependent edge recombination (τ_{eff} at the sample edge is intentionally chosen to be constant and does not depend on Δn_{av}). Also note that our simulation results are not precise for injection levels above the base-doping N$_{don}$, as R$_{base}$ is not described properly in HLI by the specific resistance of the silicon bulk. However, our simu-

lations demonstrate that the injection dependency of $\tau_{eff,av}$ in LLI can be described when only considering *majority carrier transport effects* using a simplified circuit simulation model. Such a model can therefore be used for preliminary estimation if a measured injection-dependent $\tau_{eff,av}$ might result from transport effects in combination with enhanced edge recombination.
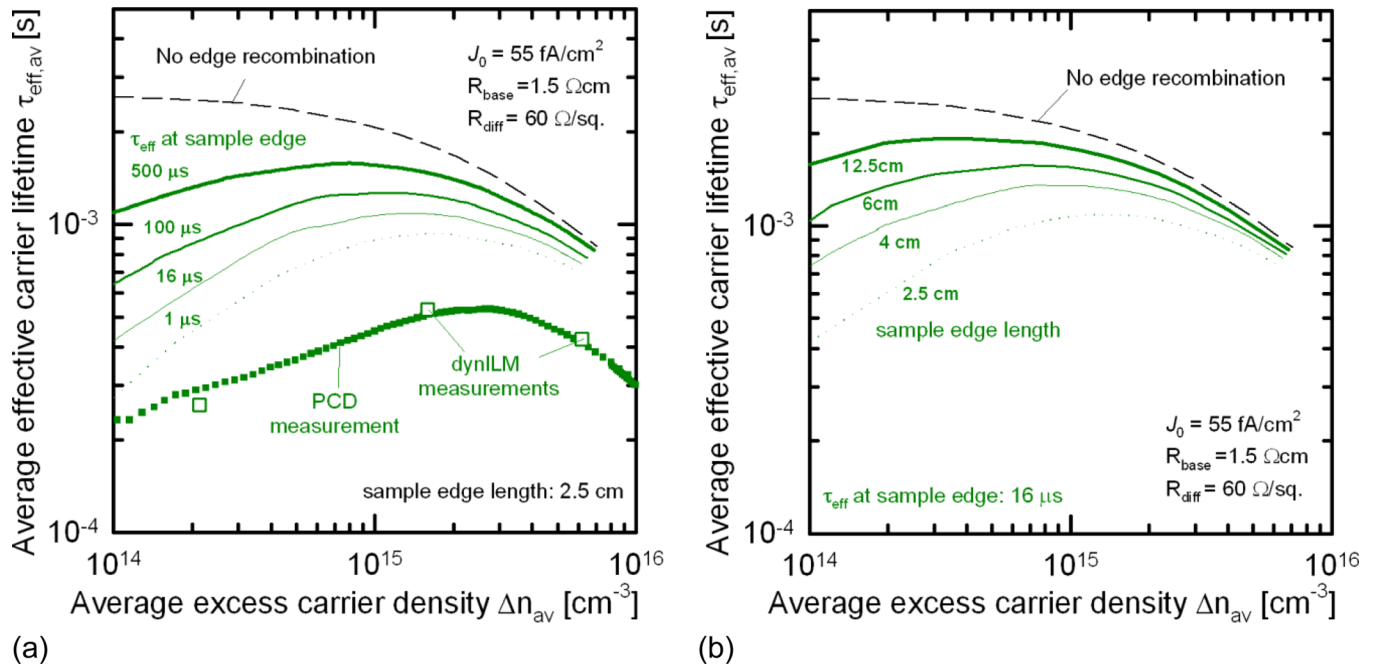

FIG. 10. (Color online) Injection-dependent $\tau_{eff,av}$ calculated with a circuit simulation of a 2.5×2.5 cm^2-sized sample with a variation of the local τ_{eff} from 1 μs to 500 μs at the sample edge (lines) and without any edge recombination at the sample edge (dashed line) (a) Injection-dependent $\tau_{eff,av}$ from circuit simulations with a variation in sample size at a local $\tau_{eff}=16$ μs at the sample edge (lines) and without any edge recombination at the sample edge (dashed line) (b).

V. CONCLUSIONS AND RECOMMENDATIONS

Consistent experimental and simulated data show a reduced averaged excess carrier lifetime $\tau_{\text{eff,av}}$ in low-level injection (LLI) in p^+np^+ samples with defect-rich edges (see Figs. 2 and 3). We show that the reduction of $\tau_{\text{eff,av}}$ is caused by (i) a high recombination rate within the space charge region (SCR) of the pn-junction at the sample edge and (ii) by the fact that both the recombining minority and majority carriers are predominantly supplied as majority currents in the p^+ and n-type regions, so the supply is drift-, but not diffusion-limited. In contrast, $\tau_{\text{eff,av}}$ is hardly affected by edge recombination in p^+pp^+ samples, because there is no pn-junction (only a high-low junction), and the electrons need to be supplied to the edges by diffusion through the p-type base region and are, hence, diffusion-limited. At high-level injection (HLI) conditions, $\tau_{\text{eff,av}}$ is hardly affected by recombination at the edges, because the fraction of recombination in the SCR decreases in respect to the overall recombination. Hence, decreased $\tau_{\text{eff,av}}$ values are measured in low-level injection if the following facts apply:

1. There is a pn-junction in the sample, either created by dopant diffusion or induced by surface charge.
2. The edges of the sample contain a significant amount of defects, typically due to laser cutting or cleaving.
3. The sample is laterally conductive to both electrons and holes, typically via the emitter (or inversion layer) and the silicon base.
4. $\tau_{\text{eff,av}}$ is determined as average over a certain area. This happens typically when the photo-conductance decay is probed by inductive coupling.
5. The recombination rate within the silicon bulk and at the front and rear surfaces is comparatively low in LLI, so the recombination in the space charge region of the pn-junction at the edges dominates the overall recombination rate.

Based on our experiments and device as well as circuit simulations, we give the following recommendations for average excess carrier lifetime measurements that are affected by sample edge recombination:

1. $\tau_{\text{eff,av}}$ in LLI should be measured on samples with a size exceeding 6×6 cm^2 (for measurements with WCT-120 lifetime tester with a coil diameter of approx. 1.8 cm) if the resistivity of the base material is below 1.5 Ωcm, the bulk excess carrier lifetime is above 1 ms, and the surfaces or diffused regions are well passivated such that $J_0 < 60$ fA/cm^2.
2. The determination of the saturation current density J_0 can be performed in samples as small as 3×3 cm^2 as long as it is performed in high-level injection conditions. The error due to edge recombination then stays below 10%.
3. Edge recombination effects, as a reason of an injection-dependent $\tau_{\text{eff,av}}$, can be tested by
   a. Locally dissolved τ_{eff} mappings for different Δn in LLI when the characteristic of τ_{eff} toward the edge does not alter significantly with a change Δn.
   b. $\tau_{\text{eff,av}} (\Delta n_{\text{av}})$ calculation with simplified circuit simulations, like presented in Sec. IV.

[1]M. Hermle, J. Dicker, W. Warta, S. W. Glunz, and G. Willeke, paper presented at the 3rd World Conference on Photovoltaics, Osaka, Japan, 12–16 May 2003.
[2]K. R. Catchpole, A. W. Blakers, and M. J. McCann, paper presented at the 17th European PVSEC, Munich, Germany, 22–26 October 2001.
[3]M. Bail, M. Schulz, and R. Brendel, Appl. Phys. Lett. **82**, 757 (2003).
[4]D. H. Neuhaus, J. P. Cousins, and A. Aberle, *Proceedings of the 3rd World Conference on Photovoltaics, Osaka, Japan, 12–16 May 2003* (2003), pp. 91–94.
[5]D. Macdonald and A. Cuevas, Sol. Energy Mater. Sol. Cells **65**, 509 (1999).
[6]M. J. Kerr and A. Cuevas, Semicond. Sci. Technol. **17**, 166 (2002).
[7]M. J. Kerr, "Surface, emitter and bulk recombination in silicon and development of silicon nitride passivated solar cells," Ph.D. dissertation, The Australian National University, 2002.
[8]S. Steingrube, P. P. Altermatt, D.S. Steingrube, J. Schmidt, and R Brendel, J. Appl. Phys. **108**, 014506 (2010).
[9]P. J. Cousins and J. E. Cotter, IEEE Trans. Electron Devices **53**, 457 (2006).
[10]S. W. Glunz, A. B. Sproul, W. Warta, and W. Wettling, J. Appl. Phys. **75**, 1611 (1994).
[11]S. Dauwe, J. Schmidt, A. Metz, and R. Hezel, *Proceedings of the 29th IEEE PVSC* (New Orleans, LA, USA, 2002), pp. 162–165.
[12]F. Kiefer, C. Ulzhöfer, T. Brendemühl, N.-P. Harder, R. Brendel, V. Mertens, S. Bordihn, C. Peters, and J. W. Müller, IEEE J. Photovoltaics **1**, 1 (2011).
[13]R. Kühn, P. Fath, and E. Bucher, *Proceedings of the 28th PVSC* (Anchorage, Alaska, USA, 2000), pp. 116–119.
[14]D. König and D. Ebest, Sol. Energy Mater. Sol. Cells **75**, 381 (2003).
[15]K. R. McIntosh and C. B. Honsberg, *Proceedings of the 16th PVSEC, Glasgow* (UK, 2000), pp. 1651–1654.
[16]S. W. Glunz, J. Dicker, M. Esterle, M. Hermle, J. Isenberg, F. J. Kamerewerd, J. Knobloch, D. Kray, A. Leimenstoll, F. Lutz, D. Oßwald, R. Preu, S. Rein, E. Schäffer, C. Schetter, H. Schmidhuber, H. Schmidt, M. Steuder, C. Vorgrimler, and G. Willeke, *Proceedings of the 29th PVSC* (New Orleans, LA, USA, 2002), pp. 450–453.
[17]M. D. Abbott, J. E. Cotter, T. Trupke, and R. A. Bardos, Appl. Phys. Lett. **88**, 114105 (2006).
[18]F. W. Chen and J. E. Cotter, Appl. Phys. Lett. **89**, 263509 (2006).
[19]K. R. McIntosh, "Lumps, humps and bumps: Three detrimental effects in the current-voltage curve of silicon solar cells," Ph.D. dissertation, University of New South Wales, 2001.
[20]R. Sinton and A. Cuevas, Appl. Phys. Lett. **69**(17), 2510 (1996).
[21]K. Ramspeck, K. Bothe, J. Schmidt, and R. Brendel, J. Appl. Phys. **106**, 114506 (2009).
[22]J. D. Plummer, M. D. Deal, and P. B. Griffin, *Silicon VLSI Technology - Fundamentals, Practice and Modeling* (Prentice-Hall, Englewood Cliffs, NJ, 2000).
[23]M. Kessler, T. Ohrdes, B. Wolpensinger, and N.-P. Harder, Semicond. Sci. Technol. **25**(5), 055001 (2010).
[24]E. Peiner, A. Schlachetzki, and D. Kruger, J. Electrochem. Soc. **142**, 576 (1995).
[25]P. Pohl, J. Schmidt, K. Bothe, and R. Brendel, Appl. Phys. Lett. **87**, 142104 (2005).
[26]H. K. Henisch and J. Zucker, Rev. Sci. Instrum. **27**, 409 (1956).
[27]D. E. Kane and R. M. Swanson, *Proceedings of the 18th IEEE PVSC, New York* (IEEE, New York, 1985), pp. 578–583.
[28]G. L. Miller, D. A. H. Robinson, and J. D. Wiley, Rev. Sci. Instrum. **47**, 799 (1976).
[29]D. K. Schroder, *Semiconductor Material and Device Characterization* (Wiley, New York, 1990).
[30]D. B. M. Klaassen, Solid-State Electron. **35**, 961 (1992).
[31]F. Dannhauser, Solid-State Electron. **15**, 1371 (1972).
[32]G. Massetti, M. Severi, and S. Solmi, IEEE Trans. Electron Devices **ED-30**, 764 (1983).
[33]J. Krausse, Solid-State Electron. **15**, 1377 (1972).

[34]*WCT-120 Photoconductance Lifetime Tester, User Manual* (Sinton Instruments, Colorado, U.S.A., 2009).

[35]W. Shockley, Bell Syst. Tech. J. **28**(3), 435 (1949).

[36]M. J. Kerr and A. Cuevas, J. Appl. Phys. **91**(4), 2473 (2002).

[37]*Sentaurus Device*, Version C-2009.06 (Synopsys Inc., Mountain View, CA, 2009).

[38]B. Hoex, J. Schmidt, R. Bock, P. P Altermatt, M. C. M. van de Sanden, and W. M. M. Kessels, Appl. Phys. Lett. **91**, 112107 (2007).

[39]P. P. Altermatt, J. Comput. Electron. **10**, 314 (2011).

[40]International Electrotechnical Commission (IEC) Standard No. 60904-3, 2008.

[41]P. P. Altermatt, A. G. Aberle, J. Zhao, A. Wang, and G. Heiser, Sol. Energy Mater. Sol. Cells **74**, 165 (2002).

[42]T. B. Stellwag, P. E. Dodd, E. S. Carpener, M. S. Lundstrom, R. F. Pierret, M. R. Melloch, E. Yablonovitch, and T. J. Gmitter, *Proceedings of the 21st IEEE PVSC* (IEEE, New York, 1990), pp. 442–447.

[43]S. Eidelloth, F. Haase, and R. Brendel, "Simulation tool for equivalent circuit modeling of photovoltaic devices," IEEE J. Photovoltaics (submitted).